Polymer Testing 140 (2024) 108580

Contents lists available at ScienceDirect

Polymer Testing

journal homepage: www.elsevier.com/locate/polytest

Structural characterization of hierarchical polymer foams by combining X-ray micro-computed tomography and scanning electron microscopy

Takumi Ono [a], Sadaki Samitsu [b,c,*], Misa Hazutani [b], Seisuke Ata [a]

[a] Research Institute for Chemical Process Technology, National Institute of Advanced Industrial Science and Technology (AIST), 1-1-1 Higashi, Tsukuba, Ibaraki, 305-8565, Japan
[b] Research Center for Macromolecules and Biomaterials, National Institute for Materials Science (NIMS), 1-2-1 Sengen, Tsukuba, Ibaraki, 305-0047, Japan
[c] Department of Nanoscience and Nanoengineering, Graduate School of Advanced Science and Engineering, Faculty of Science and Engineering, Waseda University, Japan

ARTICLE INFO

Keywords:
Polymer foam
X-ray micro-computed tomography
Scanning electron microscopy
Three dimensional imaging
Hierarchical cellular structure
Mixed blowing agent
Poly(methyl methacrylate)
Polystyrene
Macrocell

ABSTRACT

Complementary structural characterization methods are useful for studying the hierarchical cellular morphology of polymer foams. In this study, we employed scanning electron microscopy (SEM) and X-ray micro-computed tomography (micro-CT) to characterize the hierarchical cellular morphology of poly(methyl methacrylate) (PMMA) and polystyrene (PS) foams. The polymer foams were prepared using pure CO_2 gas and CO_2–chlorodifluoromethane (HCFC-22) gas mixtures as blowing agents. Depending on the type of polymer and HCFC-22 concentration, hierarchical cellular structures consisting of nanocells, microcells, and macrocells were obtained. The size distribution of the nanocells was determined by high-magnification SEM, while the size, shape, and spatial distribution of the microcells and macrocells in three dimensions were determined by micro-CT. Moreover, a well-designed micro-CT experiment enabled a brightness comparison between the foams and relative local density mapping of the foams based on the brightness. The results clearly showed the formation of a dense skin layer at the air interface of both PMMA and PS foams and dense matrix around the large macrocells in the PMMA foams. Thus, combining SEM and micro-CT provides a deeper understanding of the formation mechanism of the hierarchical cellular structure of polymer foams.

1. Introduction

Polymer foams exhibit unique physical properties, such as light weight [1], excellent strength-to-weight ratio, low thermal conductivity, good sound insulation performance [2] and high impact resistance. These properties strongly depend on cellular structure, specifically cell size, shape, connectivity, and uniformity. In general, the larger the porosity, the smaller the cell size, and the more uniform the cell structure, the better the strength-to-weight ratio and thermal insulation performance [3–6]. Light-transparent foams can be obtained by decreasing the size of nanocells to less than 50 nm, which is sufficiently smaller than the wavelength of visible light [3,7,8]. However, nanocellular foams often suffer from significant light scattering owing to the presence of macrocells, resulting in severe degradation of light transparency. To effectively suppress the unintentional generation of large macrocells, HCFC-22 can be used as a co-blowing agent with CO_2 for polymer foaming [9]. Quantitative evaluation of macrocells is important for understanding their formation mechanism and fabricating nanocellular foams with excellent optical transparency.

On the other hand, a hierarchical cellular structure consisting of nanocells, microcells, and macrocells has the advantages of sound absorption capacity [10], thermal insulation [11] and mechanical properties [12] compared to foams with a uniform cell size. Therefore, quantitative characterization of the hierarchical cellular morphology plays a key role in designing an optimal foaming process for a tailor-made cellular structure and developing polymer foams with innovative functionality. Cellular structures at the nanoscale to the microscale can be visualized by scanning electron microscopy (SEM). However, the two-dimensional images provide limited information regarding the size, shape, and spatial distribution of cells. Full three-dimensional information on cellular structures of several tens of micrometers and above can be obtained by X-ray micro-computed tomography (micro-CT) [13–18]. Although these methods have been widely used in previous studies [10–12,19], their combined use has only

---

* Corresponding author. Research Center for Macromolecules and Biomaterials, National Institute for Materials Science (NIMS), 1-2-1 Sengen, Tsukuba, Ibaraki, 305-0047, Japan.
E-mail address: SAMITSU.Sadaki@nims.go.jp (S. Samitsu).

https://doi.org/10.1016/j.polymertesting.2024.108580
Received 7 August 2024; Received in revised form 4 September 2024; Accepted 15 September 2024

been reported in one paper thus far [20]. In the paper, SEM and micro-CT are used to analyze the microstructure of poly(ε-caprolactone) foams. However, the results have not been quantitatively evaluated through combined analysis.

Here, we propose a structural characterization scheme for polymer foams with a hierarchical cellular morphology that combines digital SEM and micro-CT image analyses. Poly(methyl methacrylate) (PMMA) and polystyrene (PS) foams were prepared using pure CO_2 and CO_2–chlorodifluoromethane (HCFC-22) gas mixtures as blowing agents. The porosities of their hierarchical cellular structures were measured by SEM and micro-CT and quantitatively compared it with those determined using the Archimedes method (Fig. 1). We also determined the number, size distribution, and spatial arrangement of the macrocells. Comprehensive information on the hierarchical cellular structure can lead to a better understanding of the formation mechanisms of the nanocells, microcells, and macrocells in polymer foams.

2. Experimental

2.1. Materials

PMMA and PS were supplied by Sigma-Aldrich (USA). The molecular weights of PMMA and PS are 350,000 and 192,000 g/mol, respectively, and their densities at room temperature are 1.17 and 1.04 g/cm^3, respectively. CO_2 (99.99 % purity) and HCFC-22 (99.9 % purity) were obtained from Iwatani Corp. (Japan) and Takachiho Chemical Industrial Co., Ltd. (Japan), respectively.

2.2. Preparation of polymer foams

The PMMA foams prepared in our previous study [9] were used as foam samples. PS foams were fabricated using the same procedure, which employed pure CO_2 gas and CO_2–HCFC-22 gas mixtures as blowing agents [9]. Briefly, a PS pellet was hot-pressed into a circular disk (diameter: 8 mm; thickness: 1 mm). The disk was exposed to either high-pressure CO_2 gas or a CO_2–HCFC-22 gas mixture using a one-step high-pressure batch foaming system. The saturation temperature, pressure, and time were set to 80 °C, 40 MPa, and 24 h, respectively. Hereafter, a foam sample is denoted by a string consisting of the polymer name and molar ratio of HCFC-22 (Table 1). For example, PMMA_015 denotes a PMMA foam prepared using 1.5 mol% HCFC-22 mixed with CO_2.

Table 1
Description of poly(methyl methacrylate) (PMMA) and polystyrene (PS) foam samples.

Sample ID	Polymer	HCFC-22 (mol%)	Shape
PMMA_000[a]	PMMA	0.0	Disk
PMMA_015	PMMA	1.5	Disk
PMMA_057[a]	PMMA	5.7	Slightly deformed
PMMA_142[a]	PMMA	14.2	Severely deformed
PS_000	PS	0.0	Disk
PS_015	PS	1.5	Disk
PS_057	PS	5.7	Disk

[a] Sample fabricated in our previous study [9].

2.3. Foam characterization

The polymer foams with specific weights were characterized using the Archimedes method and SEM, as described in detail in our previous paper [9]. Density was measured by the Archimedes' method using an electric balance (Shimadzu, AP224X) and a density measurement kit (Shimadzu, SMK-601) with water as the solvent. The Archimedes porosity, ϕ_{AL}, was calculated using the following equation:

$$\phi_{AL} = \left(\frac{\rho_s - \rho_f}{\rho_s}\right) \times 100 \tag{1}$$

where ρ_s and ρ_f are the densities of the polymer disk before foaming and the foam obtained, respectively.

The cellular structure of the samples was analyzed by observing their cross section using a scanning electron microscope (S-4800, Hitachi High-Technologies Corp.). The cell size was the equivalent circle diameter calculated from the area measured using the ImageJ software [21]. The average cell size and cell size distribution were determined using at least 200 cells in the SEM micrographs.

2.4. X-ray micro-CT

Three-dimensional cellular morphology was recorded using an X-ray micro-CT system (SMX-160CTS, Shimadzu). A disk-shaped foam was cut into quarters in the radial direction and used as a specimen (approximately 5 mm in size). The tube voltage of the X-ray source was adjusted to 38–39 kV. The distance between the X-ray source and specimen was set to 20 mm, and the distance between the specimen and detector was fixed at 200 mm. Under these conditions, the entire specimen was placed in the field of view. The center of the rotation axis of the specimen was aligned, and the spatial distortion, background intensity, and offset were

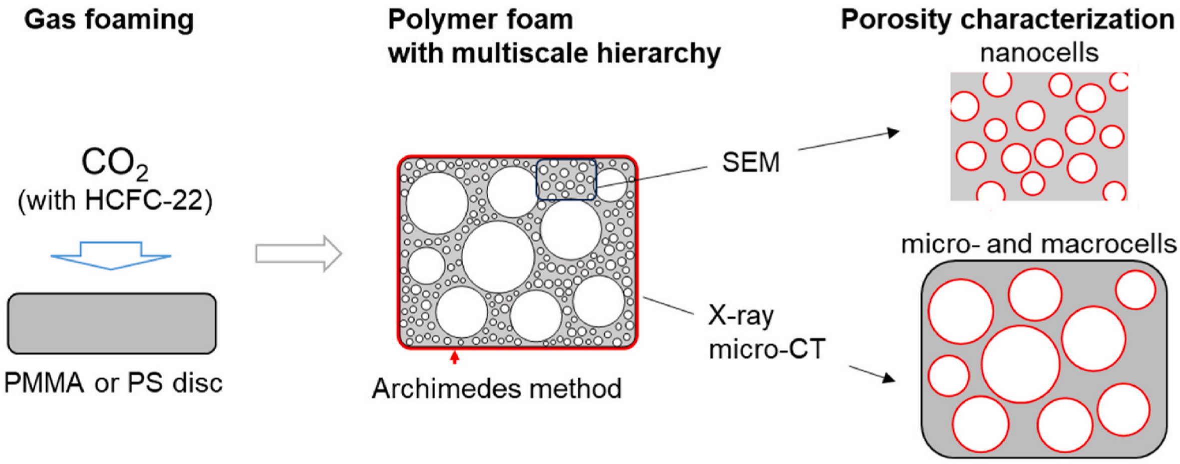

Fig. 1. Experimental procedures used in this study. Poly(methyl methacrylate) (PMMA) and polystyrene (PS) foams were blown using high-pressure CO_2 or a CO_2–chlorodifluoromethane (HCFC-22) gas mixture. The porosities of the foams were measured using the Archimedes method. The 2D and 3D cellular morphologies were characterized by cross-sectional SEM and X-ray micro-CT, respectively.

calibrated prior to the measurements. Transmission micro-CT images having 512 × 512 pixels were recorded under identical conditions using a rotation angle of 180° at 1200 steps. Raw images were reconstructed by correction using a scaling factor of 70 using the associated software of the instrument (CT-solver ver. 3.5, Shimadzu). A 3D image consisting of 512 × 512 × 512 cubic voxels was obtained, and each voxel had a brightness value of 16 bits. Microcellular morphology was recorded using a high-resolution X-ray microscope (nano3DX, Rigaku).

The CT data was analyzed using a commercial image analysis software (ExFact VR, Nihon Visual Science) with a void analysis option. The 16-bit CT data captured under the same measurement conditions were loaded by selecting the same intensity range and converted to an 8-bit brightness range. This procedure enabled a quantitative comparison of the intensities of the CT images of different samples. The total volume of a specimen, V_t, was calculated based on the apparent specimen volume, which was extracted from a 3D CT image by detecting the periphery of the specimen. A color-labeled image was created by watershed segmentation of a CT image based on a few brightness thresholds [22]. The cell size determined by micro-CT was defined as the equivalent spherical diameter calculated from the voxel-based volume of each cell. The experimental procedures used in this study are schematically illustrated in Fig. 1. In this paper, the various cells of a polymer foam are defined according to their size: <1 μm (nanocells), 1–100 μm (microcells), and >100 μm (macrocells).

3. Results and discussion

3.1. Polymer foaming and structural characterization by SEM

Fig. 2a and b shows photographs of the as-prepared PMMA disk and foamed sample PMMA_015. Foaming made the transparent PMMA disk turn white with increased thickness while retaining its shape. The porosity, ϕ_{AL}, of PMMA_015 determined using the Archimedes method was 35.6 %.

Fig. 2c and d shows the cross-sectional SEM micrographs of PMMA_015 recorded at low (× 35) and high magnifications (× 40,000). The low-magnification SEM image clearly showed several macrocells with a size range of 20–460 μm. On the other hand, the high-magnification SEM showed microcellular structures with a size range of 0.03–0.25 μm. Various locations of the sample were observed using varying magnifications (× 1000 and × 10,000), although only a few cells from a few hundred nanometers to a few micrometers were observed. The size distribution of the nanocells was determined by performing an image analysis of the high-magnification SEM micrographs (Fig. 2e). The average size, d_{SEM}^{av}, and standard deviation were respectively 0.08 μm and 0.036 μm, which is similar to those in our previous study [9]. The standard deviation normalized by the d_{SEM}^{av} was 2.2, which is higher than that obtained in a previous study on polymer foams with a similar average cell size [23].

The SEM-based porosity, ϕ_{SEM}, can be determined from the size distribution using the following equation:

$$\phi_{SEM} = \left(\frac{n}{A}\right)^{\frac{3}{2}} \frac{4}{3}\pi\left(\frac{d_{SEM}^{av}}{2}\right)^{3} \times 100 \tag{2}$$

where n is the total number of cells and A is the total area of the SEM micrographs. The ϕ_{SEM} of PMMA_015 was 2.11 %.

3.2. Micro-CT observation of macrocells

The low-magnification SEM micrograph of PMMA_015 (Fig. 2c) qualitatively confirmed the presence of several macrocells. However, the number of macrocells in the image was insufficient for statistical analysis because only one cross section of the specimen could be visualized by SEM. As researchers know, quantitatively evaluating the size and shape of macrocells by SEM is tedious and practically time-consuming. As a complementary structural characterization method to SEM, X-ray micro-CT was performed to observe the macrocells in PMMA_015 in three dimensions (Fig. 3). Micro-CT provides brightness contrast depending on the X-ray absorption intensity at each position in the field of view. Because air has a much lower density than PMMA, its lower X-ray absorption intensity caused the macrocells in the sample to appear black, as shown in the grayscale micro-CT tomogram in Fig. 3a. Segmentation based on a simple brightness threshold alone resulted in large clusters of cells. The macrocells shown in the cross-sectional SEM image of PMMA_015 appeared to be isolated from each other. In contrast, the micro-CT tomogram indicated that they were partially connected in three dimensions through narrow necks. As the clusters interfered with the measurement of the size and shape of individual cells, they were separated into cells using the watershed segmentation algorithm (Fig. S1). Optimal image processing resulted in a large number of cells appearing in multiple colors, which indicate the size ranges of the cells (Fig. 3b). Many macrocells larger than 200 μm were distributed inside the sample and appeared as red spheres. Furthermore, many microcells with sizes ranging from 20 to 50 μm could be detected as blue spheres. However, there were no macrocells at the edge of the specimen, which is the so-called skin layer [24]. The calculated number-average size of the macrocell was 58.6 μm, which was on the order of that obtained by SEM (Fig. 2c). Because of the voxel size limitation (11.8–11.9 μm in this study), the nanocells observed in the high-magnification SEM micrograph could not be visualized in the CT image.

3.3. Porosity calculated by micro-CT

The CT-based porosity, ϕ_{CT}, of a polymer foam can be calculated from the 3D CT image obtained by segmentation using the following equation:

$$\phi_{CT} = \frac{\sum v_{cell}}{V_t} \times 100 \tag{3}$$

where $\sum v_{cell}$ and V_t are the volume sum of the cells and total specimen

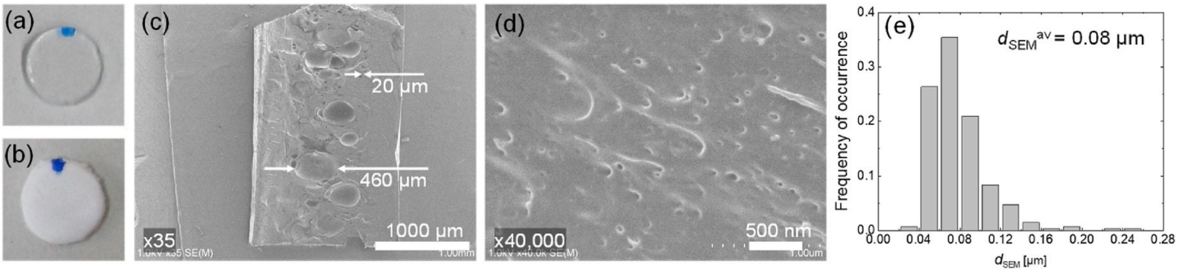

Fig. 2. Photographs of (a) a poly(methyl methacrylate) (PMMA) disk before foaming and (b) PMMA_015 obtained by foaming. Cross-sectional SEM micrographs of PMMA_015 at (c) low (× 35) and (d) high magnifications (× 40,000). (e) Size distribution of the nanocells in PMMA_015 determined from the high-magnification SEM micrograph.

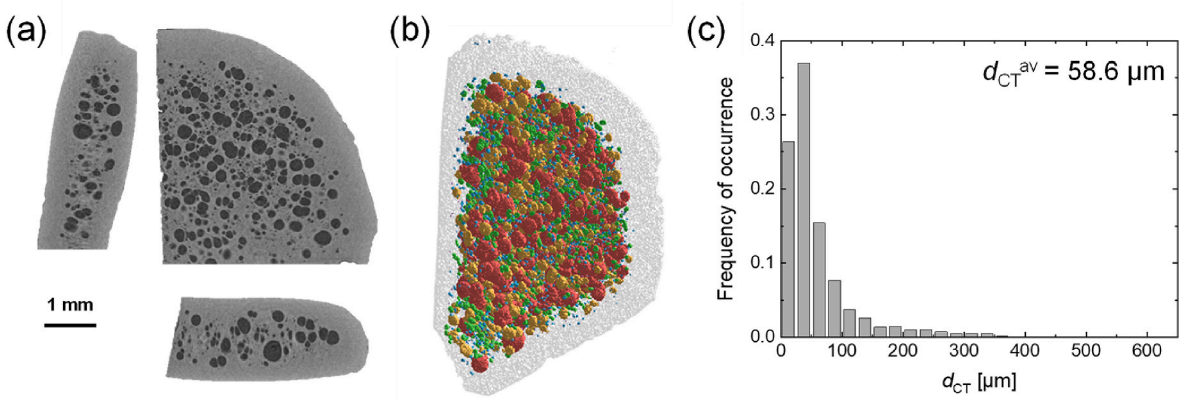

Fig. 3. (a) Grayscale X-ray micro-CT tomograms of a poly(methyl methacrylate) (PMMA) foam, PMMA_015, and (b) labeled 3D image obtained by watershed segmentation. The colors represent the cell size ranges: >200 µm (red), 100–200 µm (yellow), 50–100 µm (green), 20–50 µm (blue), and <20 µm (purple). (c) Cell size distribution of PMMA_015 determined from the CT image in (b). (For interpretation of the references to color in this figure legend, the reader is referred to the Web version of this article.)

volume, respectively. V_t can be calculated using the number of voxels in the remaining region after excluding the background region outside the specimen from the field of view of the CT image. However, in the case of a polymer foam, the brightness of the air outside the specimen often overlaps with that of the cells located inside the specimen. Thus, a simple thresholding of the voxel brightness is insufficient for determining V_t. The software used in this study has an algorithm that selectively extracts only the regions of air outside the specimen. Using the micro-CT image shown in Fig. 3b, the $\sum v_{cell}$ and V_t of PMMA_015 were determined to be 1.70×10^6 and 1.32×10^7 (voxels), respectively. Thus, the calculated ϕ_{CT} of PMMA_015 was 12.8 %, which was smaller than ϕ_{AL} (35.6 %).

3.4. Dependence of macrocell formation on the HCFC-22 molar ratio

A previous study reported the number of large macrocells decreased with increasing amount of HCFC-22 added to CO_2 using SEM analysis (Fig. S2) [9]. Here micro-CT analysis was performed to quantitatively determine the size, shape, and spatial distribution of the macrocells in polymer foams. Fig. 4 shows the grayscale micro-CT tomograms and labeled 3D images of the PMMA foams analyzed using the same procedure used for PMMA_015 (Fig. 3). As in PMMA_015, a skin layer was formed at the air interface of PMMA_000 during foaming, and numerous macrocells larger than 200 µm (shown in red in Fig. 4) were observed inside the specimen. The large macrocells of PMMA_000 and PMMA_015 had an ellipsoidal shape elongated in the thickness direction owing to

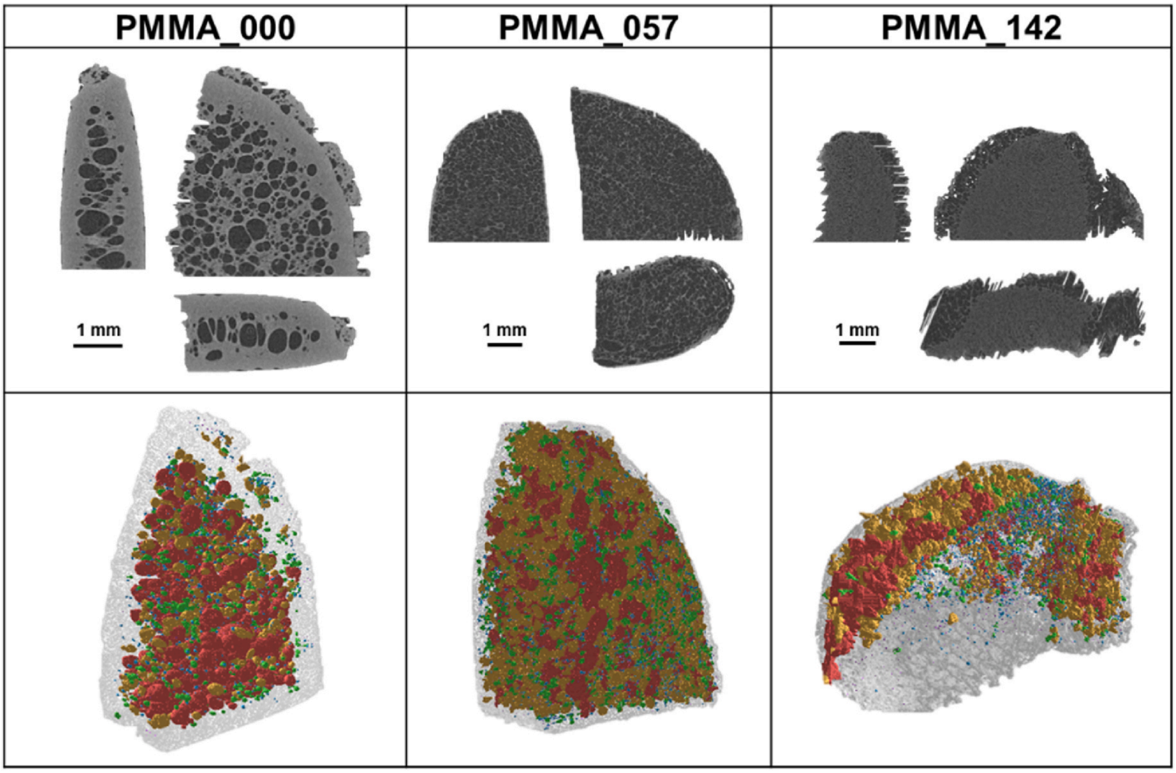

Fig. 4. Grayscale micro-CT tomograms (top) and labeled 3D images (bottom) of the poly(methyl methacrylate) (PMMA) foams, PMMA_000, PMMA_057, and PMMA_142. The colors represent the cell size ranges: >200 µm (red), 100–200 µm (yellow), 50–100 µm (green), 20–50 µm (blue), and <20 µm (purple). (For interpretation of the references to color in this figure legend, the reader is referred to the Web version of this article.)

the large expansion of the PMMA foams in nearly one direction (Fig. S3). In contrast, PMMA_057 had no skin layer, and a large number of microcells and macrocells were uniformly distributed throughout the specimen. PMMA_142 significantly collapsed, and large macrocells were generated at the air interface during foaming; however, only a few macrocells were present in the interior. Thus, using an HCFC-22 molar ratio larger than 5.7 mol% considerably deformed the disk shape of PMMA (Fig. S4). Owing to the high solubility of HCFC-22 in PMMA [25], the polymer viscosity decreased as the HCFC-22 molar ratio increased during foaming. Therefore, when HCFC-22 is mixed with CO_2 at high concentrations, PMMA foams may be unable to withstand the expansion pressure during depressurization and may lose their external shape.

3.5. Preparation and characterization of PS foams

As discussed in the previous section, PMMA foams contain numerous macrocells. PS is another polymer often used as a model polymer for CO_2 foaming because of its faster CO_2 diffusion compared to PMMA (Fig. S5) [26,27]. A different CO_2 diffusion coefficient is expected to change cell formation behavior during CO_2 foaming. Therefore, PS foams were prepared using the same procedure as that for PMMA foams, and their cellular morphology was characterized by SEM and X-ray micro-CT.

Even when foamed using a mixture of CO_2 and 5.7 mol% HCFC-22 gases, the PS foams uniformly expanded into a disk shape (Fig. 5a). In contrast to the PMMA foams, PS foams had very few macrocells, as shown in low-magnification SEM micrographs (Fig. 5b). The high-magnification SEM micrographs of all PS foams presented numerous small cells (Fig. 5c) with a size range of 0.1–1.0 μm, as calculated from the SEM micrographs (Fig. 5d). The $d_{\mathrm{SEM}}^{\mathrm{av}}$ were 0.35–0.42 μm and did not change considerably even when the amount of HCFC-22 gas changed significantly.

To examine the macrocells in detail, the PS foams were imaged by micro-CT using the same method used for PMMA_015 (Fig. 3). Their grayscale CT tomograms and labeled 3D images are shown in Fig. 6. The SEM micrographs of the PS foams showed a few macrocells, whereas the CT images confirmed the presence of a moderate number of macrocells in the specimens. The macrocells in PS_000 were mostly located at the side edge, whereas those in PS_015 were concentrically aligned at the side edge. PS_057 had a sparse distribution of microcells and small macrocells in its interior. The size distribution of the macrocells evaluated by micro-CT is shown in Fig. S6. The PS foamed using pure CO_2 gas, PS_000, had 20 % of the number density of macrocells in PMMA_000. When HCFC-22 was added to CO_2, the number density increased for PMMA but decreased for PS. Consequently, the number density of macrocells in PS_057 was only 2 % of that in PMMA_057. Thus, X-ray micro-CT is useful for characterizing a small number of macrocells in a polymer foam.

3.6. Relationship between porosities calculated using the Archimedes method, SEM, and micro-CT

The porosities and average cell sizes obtained by SEM and micro-CT are summarized in Table 2. In contrast to ϕ_{AL}, which accounts for all the cells in a sample independent of the cell size, ϕ_{CT} reflects only the cells that can be detected by micro-CT (Fig. 1), which are several tens of micrometers or larger owing to the size limit of the voxel used in this study. SEM can be used to visualize cell structures from the nanoscale to the microscale in two dimensions and determine the porosity derived from nanocells.

ϕ_{AL} was plotted against the sum of the SEM- and micro-CT-based porosities, $\phi_{\mathrm{SEM+CT}}$ (Fig. 7). The closer $\phi_{\mathrm{SEM+CT}}$ is to the diagonal of the plot, the better the agreement with ϕ_{AL}. Most of PMMA and PS foams exhibited a $\phi_{\mathrm{SEM+CT}}$ smaller than ϕ_{AL}. The PS foams had only a few macrocells, and ϕ_{CT} was less than 1 % (Table 2). Thus, ϕ_{SEM} agreed well with ϕ_{AL}. The PMMA foams with a skin layer, PMMA_000 and PMMA_015, had a relatively small ϕ_{CT} of 12–16 %, and their $\phi_{\mathrm{SEM+CT}}$ was also close to ϕ_{AL}. These foams were well-formed disks with large macrocells; macrocells smaller than 200 μm accounted for only 22–28 % of ϕ_{CT} (Fig. S7). On the other hand, the $\phi_{\mathrm{SEM+CT}}$ of PMMA_057 and PMMA_142 were quite off-diagonal and much smaller than ϕ_{AL}. These foams significantly lost their disk shape during foaming and contained many microcells and small macrocells; macrocells smaller than 200 μm accounted for more than 50 % of ϕ_{CT} (Fig. S7). As the size of the microcell approaches the voxel size in a micro-CT image, the boundary

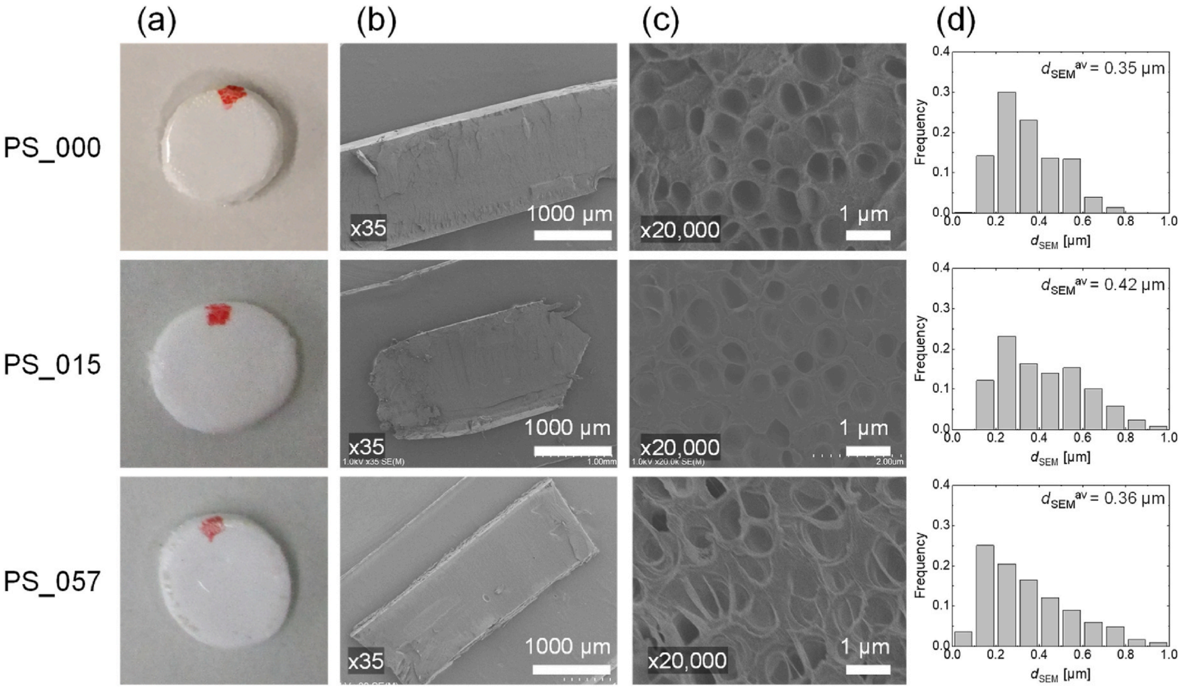

Fig. 5. (a) Photographs of the polystyrene (PS) foams, PS_000, PS_015, and PS_057. Cross-sectional SEM micrographs of the PS foams at (b) low (× 35) and (c) high magnifications (× 20,000). (d) Size distribution of the nanocells in the PS foams determined from the high-magnification SEM micrographs.

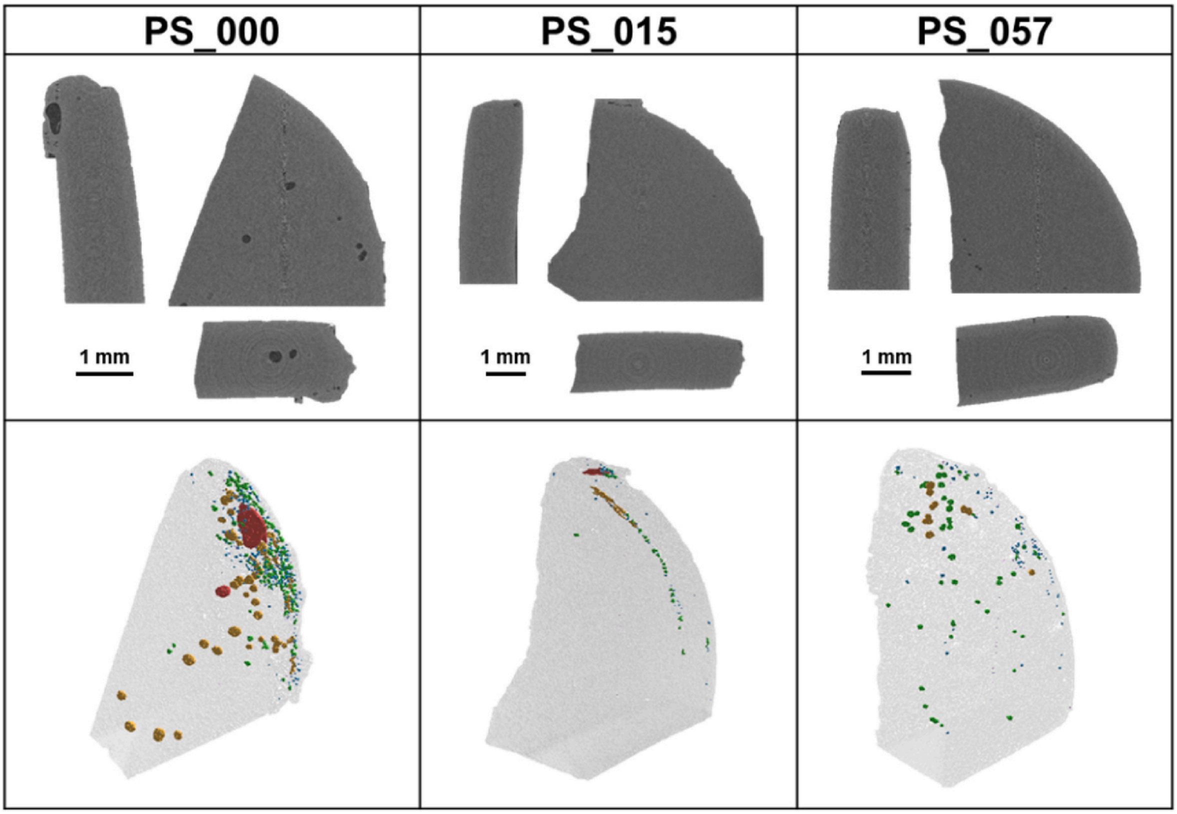

Fig. 6. Grayscale micro-CT tomograms (top) and labeled 3D images (bottom) of the polystyrene (PS) foams, PS_000, PS_015, and PS_057. The colors represent the cell size ranges: >200 μm (red), 100–200 μm (yellow), 50–100 μm (green), 20–50 μm (blue), and <20 μm (purple). (For interpretation of the references to color in this figure legend, the reader is referred to the Web version of this article.)

Table 2
Cellular structure parameters (porosity ϕ and average cell size d^{av}) of poly (methyl methacrylate) (PMMA) and polystyrene (PS) foams.

Sample	ϕ_{AL} (%)	ϕ_{SEM} (%)	ϕ_{CT} (%)	N_0 (mm^{-3})[a]	d^{av}_{SEM} (μm)	d^{av}_{CT} (μm)
PMMA_000	41.3[b]	0.5	15.7	130.1	0.09[b]	69.3
PMMA_015	35.6	2.1	12.8	179.7	0.08	58.6
PMMA_057	82.8[b]	5.7	37.2	330.6	0.22[b]	87.1
PMMA_142	85.1[b]	22.8	15.5	204.0	0.35[b]	56.0
PS_000	34.6	19.0	0.8	26.4	0.35	47.3
PS_015	22.7	28.5	0.1	4.9	0.42	38.0
PS_057	35.1	30.8	0.1	8.1	0.36	41.8

[a] Number density of voids determined by micro-CT.
[b] Values reported in our previous paper [9].

between the cell and matrix is obscured by the partial volume effect in the voxel image [28]. In this case, the calculated cell volume is smaller than the actual volume. This discrepancy can be significantly reduced by visualizing micro-CT images using voxel sizes that are sufficiently smaller than the size of the macrocells to be evaluated.

The PMMA foams with high ϕ_{AL}, PMMA_057 and PMMA_142, were observed using a high-resolution X-ray microscope with a voxel size of 2.5 μm (Fig. S8). In PMMA_057, numerous macrocells with sizes ranging from 100 to 300 μm were observed, with very thin cell walls less than 10 μm thick. PMMA_142 contained microcells with sizes of 10–40 μm. The cellular morphology appeared similar in the micro-CT tomograms shown in Fig. 4. However, X-ray microscopy provided better contrast and a smaller voxel size, which allowed for clearer images of the fine cellular morphology of the polymer foams (Fig. S9). The porosities calculated from the X-ray microscopy images were higher than those calculated from the micro-CT images. Therefore, $\phi_{SEM + CT}$ agreed better with ϕ_{AL}, particularly for PMMA_057 (Fig. 7). For foams with multiscale

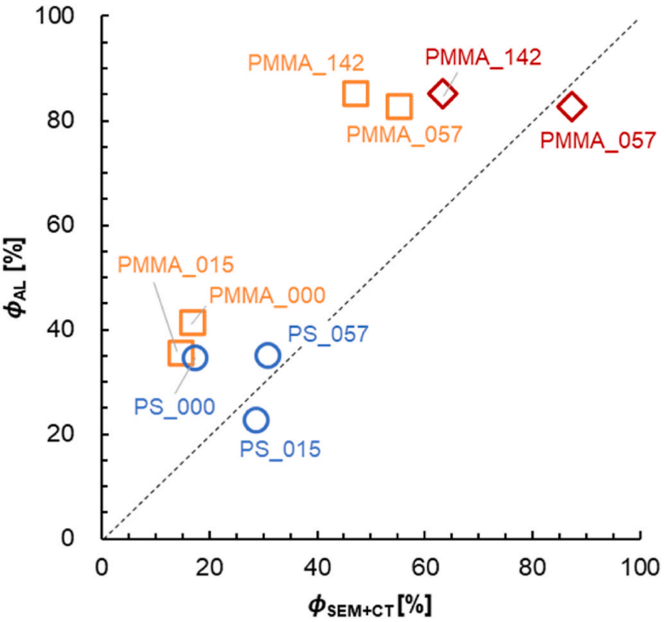

Fig. 7. Plot of the Archimedes porosity, ϕ_{AL}, versus the sum of SEM- and micro-CT-based porosities, $\phi_{SEM + CT}$. The circles represent the porosities of polystyrene (PS) foams. The squares and diamonds represent the porosities of poly (methyl methacrylate) (PMMA) foams calculated from the volume data using voxel sizes of 11.8–11.9 (X-ray micro-CT) and 2.5 μm (X-ray microscopy), respectively.

hierarchy, neither SEM nor X-ray micro-CT alone provided sufficient information on the cellular structure. A deeper understanding can be obtained by combining structural analysis methods that employ different spatial scales.

3.7. High-density layer in the skin and around the large macrocells visualized with micro-CT

To gain insight into the foaming mechanism in terms of the release of blowing agent, the histogram of the voxel brightness in the micro-CT images was analyzed in detail (Fig. 8a). Voxel brightness reflects the local density of the specimen. When CT images are recorded using the same instrument under the same conditions, the brightness values of samples made of the same material can be compared. The histogram of PMMA_000 showed two clear peaks. The plateau between the small and large peaks in the histogram resulted from the partial volume effect, which is typical in X-ray micro-CT. The small peak was well fitted to a Gaussian curve with a brightness peak, I_{air}, of 63 because X-ray CT usually records the voxel brightness distribution as a Gaussian distribution [28]. The large peak, on the other hand, could not be fitted to a single Gaussian curve owing to the overlay of a weak shoulder at the higher-brightness region. However, the peak was well fitted to an overlay of two Gaussian curves with a lower-brightness peak, I_{LM}, of 124 and higher-brightness peak, I_{HM}, of 134 (Fig. S10). The threshold value for the plateau between small and large peaks was set to 94 in the imaging software based on the Cross L standard.

Using two brightness thresholds, the grayscale micro-CT tomograms of PMMA_000 shown in Fig. 4 were divided into three regions, which are displayed in different colors in Fig. 8b. Brightness values of 94 and below are colored purple, 94–131 are yellow, and 131 and above are red. The purple region represents the lowest brightness corresponding to air, that is, macrocells in the foam. The yellow region located inside the specimen represents the nanocellular matrix. Although no cells were observed in the yellow region of the micro-CT image, the presence of nanocells was confirmed by SEM (Fig. S2). The red region located at the air interface, which has a thickness of 100–220 μm, corresponds to the skin layer of the foam. The skin layer had a higher density than the nanocellular matrix because it generated microcells hardly and less numbers of nanocells owing to the immediate release of the blowing agent during foaming. Interestingly, a high-density region (red) was also clearly observed around the macrocells, as shown in the enlarged CT tomogram (Fig. 8c). The increase in local density was more pronounced in the vicinity of the larger macrocells. The similarity to the skin layer suggests that fewer microcells and nanocells formed in the vicinity of the macrocells, resulting in a higher density than the nanocellular matrix. This is presumably because the macrocells preferentially absorb the surrounding dissolved gases, reducing the number of nanocells. X-ray micro-CT measurements can visualize the relative density differences within a sample in three dimensions, which may be useful to experimentally verify the macrocell formation mechanism proposed so far.

Using the same procedure, the brightness histograms of the micro-CT images of all polymer foams (Fig. S11) were fitted to three Gaussian curves to obtain the three brightness peaks, I_{air}, I_{LM}, and I_{HM}, which are summarized in Table S1. I_{LM}, which corresponds to the nanocellular matrix (yellow region), decreased as ϕ_{SEM} increased (Fig. S12). This trend did not apply to PMMA_057 and PMM_142, whose I_{LM} were smaller than expected owing to the partial volume effect in micro-CT caused by insufficient voxel size, as discussed in Section 3.6. Because brightness correlates with the local electron density, I_{LM} decreased as the number of nanocells increased, even if each individual nanocell could not be visualized by micro-CT. Because PMMA and PS have different mass absorption coefficients and true densities, they had slightly different CT brightness values for the same ϕ_{SEM}.

Using the same procedure used for PMMA_000, the micro-CT tomograms of the PMMA foams blown using CO_2–HCFC-22 gas mixtures were labeled using three colors (Fig. 9). At low amounts of HCFC-22 (PMMA_000 and PMMA_015), the foaming gas near the surface was rapidly released from the sample, creating a skin layer near the surface and microcells inside the sample. Macrocells can be generated by the excessive growth of a small number of microcells because of their inability to release gases inside the polymer. PMMA_057 uniformly generated many microcells and small macrocells throughout the sample, resulting in a large ϕ_{CT}. The significant amount of gases dissolved in PMMA_142 caused a significant decrease in polymer viscosity, and PMMA_142 collapsed owing to the expansion pressure during depressurization. Consequently, most of the gas was released from the sample before the macrocells grew, and large macrocells appeared only near the surface.

The micro-CT tomograms of the PS foams were also labeled using three colors (Fig. 10). The colored tomograms confirmed the presence of a skin layer near the sample surface, which is represented by the red region with a high CT brightness. Because the diffusion rate of CO_2 in PS is significantly higher than that in PMMA, the dissolved gas quickly escaped from the sample. The quick release of gas created a skin layer on the surface and prevented macrocells from forming inside the sample.

4. Conclusions

PMMA and PS foams were prepared using pure CO_2 gas and CO_2–HCFC-22 gas mixtures as blowing agents. They had a hierarchical cellular morphology consisting of nanocells, microcells, and macrocells. The nanocells had average sizes of 0.08–0.42 μm depending on type of polymer and HCFC-22 molar ratio, as determined from the high-magnification SEM images. Micro-CT is useful for characterizing microcells and macrocells in polymer foams because it provides full information on their size, shape, and spatial distribution. The PMMA foams had large macrocells at low HCFC-22 concentrations, and the macrocell size decreased with increasing HCFC-22 concentration. The PS foams exhibited a smaller number of macrocells owing to the faster diffusion of CO_2.

When CT images are recorded using the same instrument under the same conditions, the voxel brightness of samples made of the same

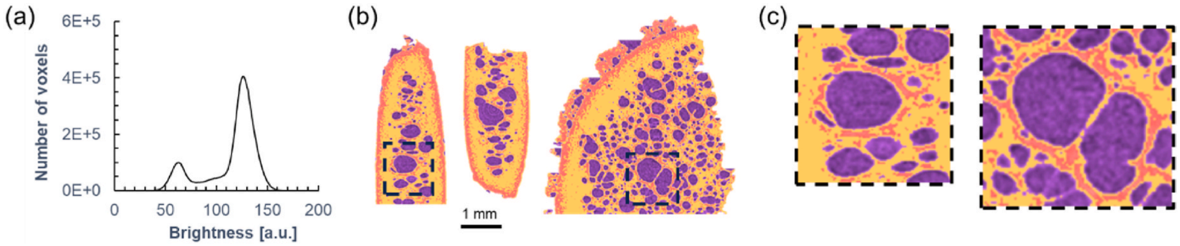

Fig. 8. (a) Brightness histogram of a CT image of a poly(methyl methacrylate) (PMMA) foam, PMMA_000. The histogram is fitted to three Gaussian curves and divided into three regions based on brightness thresholds. (b) Micro-CT tomograms of PMMA_000 displayed in three colors according to voxel brightness: ≤94 (purple), 94–131 (yellow), and ≥131 (red). (c) Enlarged views of the areas enclosed by the broken line in (b). (For interpretation of the references to color in this figure legend, the reader is referred to the Web version of this article.)

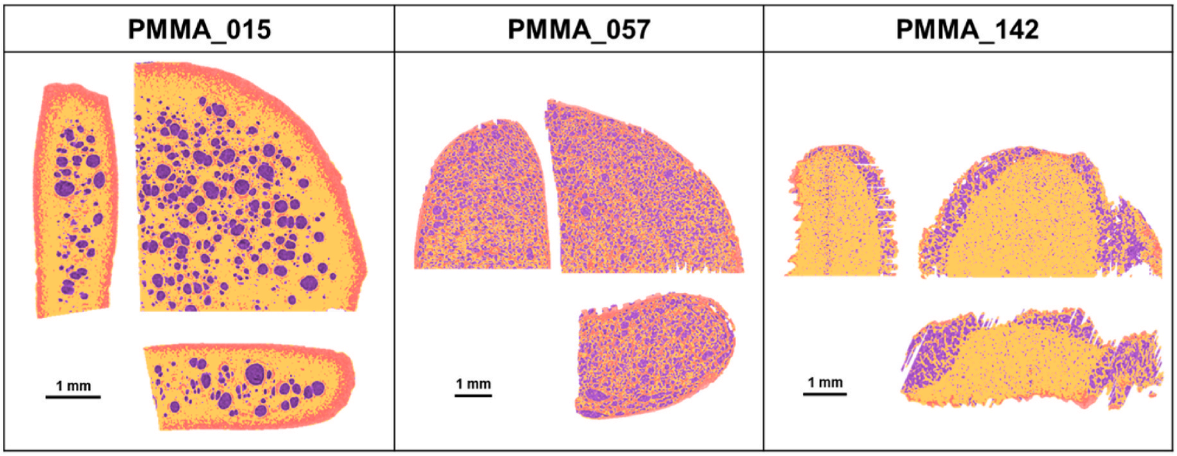

Fig. 9. Micro-CT tomograms of poly(methyl methacrylate) (PMMA) foams labeled using three colors based on voxel brightness: low (purple), medium (yellow), and high (red). (For interpretation of the references to color in this figure legend, the reader is referred to the Web version of this article.)

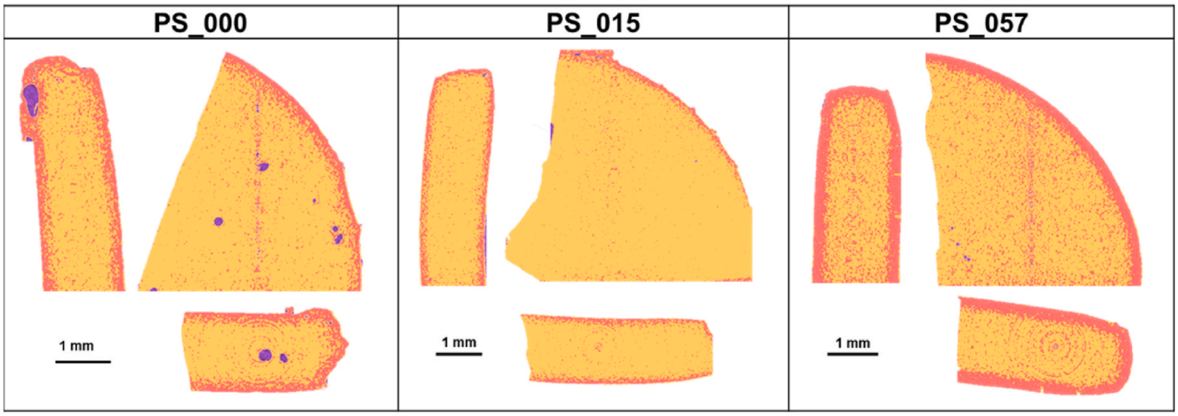

Fig. 10. X-ray micro-CT tomograms of polystyrene (PS) foams labeled using three colors based on voxel brightness: low (purple), medium (yellow), and high (red). (For interpretation of the references to color in this figure legend, the reader is referred to the Web version of this article.)

material can be compared and correlated with the matrix density. An air interface with a thickness of 100–220 μm, corresponding to the skin layer of the polymer foams, had higher brightness and no macrocells. Similar bright regions were also observed around the large macrocells, indicating that the macrocells preferentially absorbed the surrounding dissolved gases, and the number of nanocells decreased around the large macrocells. X-ray micro-CT measurements can provide relative density distributions within a foam in three dimensions and may also be useful to obtain experimental evidence to understand the mechanism of macrocell formation.

For polymer foams with a multiscale hierarchy, the complementary information on cellular morphology provided by SEM and X-ray micro-CT allows a deeper understanding of the formation mechanism and provides additional insight into the process design for tailor-made polymer foams.

CRediT authorship contribution statement

Takumi Ono: Writing – review & editing, Writing – original draft, Validation, Methodology, Investigation, Funding acquisition, Conceptualization. **Sadaki Samitsu:** Writing – review & editing, Writing – original draft, Validation, Methodology, Investigation, Funding acquisition, Conceptualization. **Misa Hazutani:** Investigation, Data curation. **Seisuke Ata:** Writing – review & editing, Writing – original draft, Validation, Methodology, Investigation, Funding acquisition, Conceptualization.

Declaration of competing interest

The authors declare the following financial interests/personal relationships which may be considered as potential competing interests:

The project was financially supported by Tsukuba Innovation Arena (Director: Takumi Ono, who is one of the co-authors of this manuscript).

Data availability

Data will be made available on request.

Acknowledgements

The authors thank Ms. Akiko Takenouchi and Dr. Makoto Watanabe of the National Institute for Materials Science (NIMS) for their assistance with the X-ray micro-CT system and Prof. Dr. Masanobu Naito of NIMS for his assistance with the X-ray microscope. This research was supported by the Tsukuba Innovation Arena (TIA) collaborative research program, “Kakehashi,” in Japan, in 2022.

Appendix A. Supplementary data

Supplementary data to this article can be found online at https://doi.org/10.1016/j.polymertesting.2024.108580.

References

[1] M. Haurat, M. Sauceau, F. Baillon, L. Le Barbenchon, M. Pedros, M. Dumon, Supercritical CO2-assisted extrusion foaming: a suitable process to produce very lightweight acrylic polymer micro foams, J. Appl. Polym. Sci. 140 (2023) e532277, https://doi.org/10.1002/app.53277.

[2] G. Wang, G. Zhao, G. Dong, Y. Mu, C.B. Park, G. Wang, Lightweight, super-elastic, and thermal-sound insulation bio-based PEBA foams fabricated by high-pressure foam injection molding with mold-opening, Eur. Polym. J. 103 (2018) 68–79, https://doi.org/10.1016/j.eurpolymj.2018.04.002.

[3] C. Forest, P. Chaumont, P. Cassagnau, B. Swoboda, P. Sonntag, Polymer nano-foams for insulating applications prepared from CO2 foaming, Prog. Polym. Sci. 41 (2015) 122–145, https://doi.org/10.1016/j.progpolymsci.2014.07.001.

[4] B. Notario, J. Pinto, E. Solorzano, J.A. de Saja, M. Dumon, M.A. Rodríguez-Pérez, Experimental validation of the Knudsen effect in nanocellular polymeric foams, Polymer 56 (2015) 57–67, https://doi.org/10.1016/j.polymer.2014.10.006.

[5] J. Martín-de León, F. Van Loock, V. Bernardo, N.Á. Fleck, M.A. Rodríguez-Pérez, The influence of cell size on the mechanical properties of nanocellular PMMA, Polymer 181 (2019) 121805, https://doi.org/10.1016/j.polymer.2019.121805.

[6] R. Zhang, J. Chen, Y. Zhu, J. Zhang, G. Luo, P. Cao, Q. Shen, L. Zhang, Correlation between the structure and compressive property of PMMA microcellular foams fabricated by supercritical CO2 foaming method, Polymers 12 (2020) 315, https://doi.org/10.3390/polym12020315.

[7] H. Yokoyama, L. Li, T. Nemoto, K. Sugiyama, Tunable nanocellular polymeric monoliths using fluorinated block copolymer templates and supercritical carbon dioxide, Adv. Mater. 16 (2004) 1542–1546, https://doi.org/10.1002/adma.200400072.

[8] J. Martín-de León, J.L. Pura, V. Bernardo, M.Á. Rodríguez-Pérez, Transparent nanocellular PMMA: characterization and modeling of the optical properties, Polymer 170 (2019) 16–23, https://doi.org/10.1016/j.polymer.2019.03.010.

[9] T. Ono, T. Furuya, H. Niino, S. Yoda, Nanocellular foaming of poly (methyl methacrylate) with chlorodifluoromethane (HCFC-22)/CO2 binary mixtures as a model blowing agent, J. Supercrit. Fluids 181 (2022) 105502, https://doi.org/10.1016/j.supflu.2021.105502.

[10] S.G. Mosanenzadeh, H.E. Naguib, C.B. Park, N. Atalla, Development of polylactide open-cell foams with bimodal structure for high-acoustic absorption, J. Appl. Polym. Sci. 131 (2014) 39518, https://doi.org/10.1002/app.39518.

[11] C.L. Zhang, B. Zhu, D.C. Li, L.J. Lee, Extruded polystyrene foams with bimodal cell morphology, Polymer 53 (2012) 2435–2442, https://doi.org/10.1016/j.polymer.2012.04.006.

[12] J.-B. Bao, G.-S. Weng, L. Zhao, Z.-F. Liu, Z.-R. Chen, Tensile and impact behavior of polystyrene microcellular foams with bi-modal cell morphology, J. Cell. Plast. 50 (2014) 381–393, https://doi.org/10.1177/0021955x14525960.

[13] S. Pérez-Tamarit, E. Solórzano, R. Mokso, M.A. Rodríguez-Pérez, In-situ understanding of pore nucleation and growth in polyurethane foams by using real-time synchrotron X-ray tomography, Polymer 166 (2019) 50–54, https://doi.org/10.1016/j.polymer.2019.01.049.

[14] C. Timpano, H. Abdoli, S.N. Leung, G.W. Melenka, Characterization of open-cellular polymeric foams using micro-computed tomography, Polymer 202 (2020) 122628, https://doi.org/10.1016/j.polymer.2020.122628.

[15] L.M. Borgmann, S. Johnsen, C.S. de Oliveira, J.M. de Souza e Silva, J. Li, C. Kirchlechner, G. Gomard, G. Wiegand, H. Höelscher, Porous polymeric microparticles foamed with supercritical CO2 as scattering white pigments, Bioinspiration Biomimetics 18 (2023) 026011, https://doi.org/10.1088/1748-3190/acb899.

[16] X.C. Zhu, Z.K. Cheng, Y.M. Chen, Thickness measurement of cell walls of closed-cell foams in micro-CT images, J. Microsc. 291 (2023) 145–155, https://doi.org/10.1111/jmi.13190.

[17] N. Sakata, Y. Takeda, M. Kotera, Y. Suzuki, A. Matsumoto, Interfacial structure control and three-dimensional X-ray imaging of an epoxy monolith bonding system with surface modification, Langmuir 36 (2020) 10923–10932, https://doi.org/10.1021/acs.langmuir.0c01481.

[18] R. Tominaga, Y. Takeda, M. Kotera, Y. Suzuki, A. Matsumoto, Non-destructive observation of internal structures of epoxy monolith and co-continuous network polymer using X-ray CT imaging for elucidation of their unique mechanical features and fracture mechanism, Polymer 263 (2022) 125433, https://doi.org/10.1016/j.polymer.2022.125433.

[19] K. Güzel, J.C. Zarges, H.P. Heim, Effect of cell morphology on flexural behavior of injection-molded microcellular polycarbonate, Materials 15 (2022), https://doi.org/10.3390/ma15103634.

[20] M. Karimi, M. Heuchel, T. Weigel, M. Schossig, D. Hofmann, A. Lendlein, Formation and size distribution of pores in poly(ε-caprolactone) foams prepared by pressure quenching using supercritical CO2, J. Supercrit. Fluids 61 (2012) 175–190, https://doi.org/10.1016/j.supflu.2011.09.022.

[21] C.A. Schneider, W.S. Rasband, K.W. Eliceiri, NIH Image to ImageJ: 25 years of image analysis, Nat. Methods 9 (2012) 671–675, https://doi.org/10.1038/nmeth.2089.

[22] C. Couprie, L. Grady, L. Najman, H. Talbot, Power watersheds: a new image segmentation framework extending graph cuts, random walker and optimal spanning forest, in: IEEE 12th International Conference on Computer Vision, Kyoto, Japan, 2009, pp. 731–738, https://doi.org/10.1109/ICCV.2009.5459284.

[23] V. Bernardo, J. Martin-de Leon, E. Laguna-Gutierrez, T. Catelani, J. Pinto, A. Athanassiou, M.A. Rodriguez-Perez, Understanding the role of MAM molecular weight in the production of PMMA/MAM nanocellular polymers, Polymer 153 (2018) 262–270, https://doi.org/10.1016/j.polymer.2018.08.022.

[24] S.K. Goel, E.J. Beckman, Generation of microcellular polymeric foams using supercritical carbon dioxide. II: cell growth and skin formation, Polym. Eng. Sci. 34 (1994) 1148–1156, https://doi.org/10.1002/pen.760341408.

[25] D. Boudouris, J. Prinos, M. Bridakis, M. Pantoula, C. Panayiotou, Measurement of HCFC-22 and HFC-152a sorption by polymers using a quartz crystal microbalance, Ind. Eng. Chem. Res. 40 (2001) 604–611, https://doi.org/10.1021/ie000382h.

[26] I. Ushiki, S. Hayashi, S. Kihara, S. Takishima, Solubilities and diffusion coefficients of carbon dioxide and nitrogen in poly(methyl methacrylate) at high temperatures and pressures, J. Supercrit. Fluids 152 (2019) 104565, https://doi.org/10.1016/j.supflu.2019.104565.

[27] Y. Sato, T. Takikawa, S. Takishima, H. Masuoka, Solubilities and diffusion coefficients of carbon dioxide in poly(vinyl acetate) and polystyrene, J. Supercrit. Fluids 19 (2001) 187–198, https://doi.org/10.1016/S0896-8446(00)00092-9.

[28] M. Kato, M. Takahashi, S. Kawasaki, T. Mukunoki, K. Kaneko, Evaluation of porosity and its variation in porous materials using microfocus X-ray computed tomography considering the partial volume effect, Mater. Trans. 54 (2013) 1678–1685, https://doi.org/10.2320/matertrans.M-M2013813.